A semiconductor 96-microplate platform for real-time impedance-based high-throughput screening

Shalaka Chitale[1], Wenxuan Wu[1,2], Avik Mukherjee[3], Herbert Lannon[1], Pooja Suresh[1], Ishan Nag[1], Christina Ambrosi[1], Rona S. Gertner[4], Hendrick Melo[1], Brendon Powers[1], Hollin Wilkins[1], Henry Hinton[2], Mickey Cheah[1], Zachariah Boyton[1], Alexander Alexeyev[1], Duane Sword[1], Markus Basan[3], and Hongkun Park[4,5,*], Donhee Ham[2,*], Jeffrey Abbott[1,2,4,5,*]

[1]CytoTronics Inc., Boston, MA, USA.

[2]John A. Paulson School of Engineering and Applied Sciences, Harvard University, Cambridge, MA, USA.

[3]Department of System Biology, Harvard Medical School, Boston, Massachusetts, USA.

[4]Department of Chemistry and Chemical Biology, Harvard University, Cambridge, Massachusetts, USA.

[5]Department of Physics, Harvard University, Cambridge, Massachusetts, USA.

*To whom correspondence should be addressed: donhee@seas.harvard.edu, hongkun_park@harvard.edu, and jabbott@cytotronics.com

Abstract

Recent advancements in high-throughput screening have focused on using multi-parametric readouts to characterize drug compound effects. While high-content imaging is commonly used, it only captures endpoint images of fixed cells. Here, we report a semiconductor 96-microplate platform which performs real-time, label-free impedance "imaging" of live-cells. An array of 64×64=4,096 electrodes/well provides spatial resolution of 25 μm and enables multi-frequency, field-based measurements to capture >20 morphological and functional parameters. This represents a major advancement over current electronic microplates which use 2 electrodes/well for single parameter measurement. Unique characteristics including tissue barrier, cell-surface attachment, transepithelial water transport, cell size and motility are captured every 5-15 min during the experiment time-course. Eleven cell types ranging from primary epithelial to suspension are functionally characterized and proof-of-concept screens using 341 FDA approved compounds highlight the ability to perform mechanism of action (MOA) profiling. Compounds increasing tissue barrier with a previously unreported MOA were identified, an illustrative example of phenotypic discovery in the context of gut barrier diseases. The combination of MOA profiling and direct translatability of functional phenotypes promises to unlock new avenues in phenotypic high-throughput screening.

Introduction

High-throughput screening is the dominant paradigm for profiling compounds based on biological activity, toxicity, and mechanism of action (MOA)[1]. One of the most informative screening tools is high-content imaging with feature extraction to create high-dimensional profiles (e.g., Cell Painting[2]). However, the technique only produces an end-point image of fluorescently labeled fixed cells, missing important characteristics of live cells and tissues. Most notably, barrier and water transport properties of epithelia are critical for cancer[3], fibrosis[4], inflammation[5], and cystic diseases[6,7], yet they cannot be assessed using high-content imaging.

Impedance techniques can complement the shortcomings of imaging, providing live-cell morphology information – such as epithelial barrier properties – in real time, throughout the full experiment time-course. Moreover, they bring the additional advantages of being non-invasive and label-free[8], enabling experiments without fluorescent probes or cell line engineering. These impedance techniques include transepithelial electrical resistance (TEER) assays[9] and other commercial devices (e.g., xCelligence RTCA[10] by Agilent Technologies, Inc., ECIS[11] by Applied Biophysics, Inc.) which measure the impedance of cell membranes to examine tissue barrier and kinetics (cell growth/death). Nonetheless, these devices use large electrode pairs for measurement resulting in limitations in both accuracy and the number/type of parameter readouts. Consumer electronic semiconductor technology offers a solution to these challenges by integrating thousands of electrodes at cellular resolutions[12]. Yet to date, only single well prototypes have been reported. For the impedance techniques to genuinely complement high-content imaging and for their benefit to be fully materialized, they should be provided not only in high-resolution (thus high-accuracy) as in Ref. 12, but also in high-throughput.

Here, we report a high-throughput, high-resolution impedance platform for drug discovery applications and demonstrate its ability for high-dimensional MOA profiling through live-cell morphology responses and phenotypic hit/lead generation. We integrate semiconductor microchips into each well of a 96-well plate to provide a spatial accuracy of 25 µm, enable scalability through 8× parallel plate (768 wells) operation within incubators, and create high-dimensional readouts. The 20+ parameters generated from different frequencies, field geometries, and spatial features measured across the 4,096 electrodes/well significantly expands capabilities of classic impedance tools, which typically measure only one[10] or two[11] parameters between 2 electrodes/well. By acquiring these parameters every 5-15 min in real-time, we obtain a full kinetic view of live-cell growth and compound responses, providing functional insights beyond end-point imaging.

The sensitivity and diversity of the measurements create a high-dimensional electrical representation of cell state over time, which we have highlighted in the characterization of eleven different cell types ranging from primary epithelial, to cancer epithelial, to suspension; each with unique morphology and growth dynamics. Through proof-of-concept screens of 341 FDA approved compounds, the platform shows promise for the real-time, label-free profiling of compound MOA on live-cells. In addition, the translatability of the unique parameters unlocks phenotypic high-throughput screening for related drug discovery applications, including epithelial to mesenchymal transition (EMT), transepithelial water transport, and barrier function. The identification of previously unknown compounds that increase tissue barrier highlights the ability of the platform for finding novel therapeutic approaches in the context of gut barrier diseases.

Results

Design and optimization of a 96 well CMOS plate, high throughput platform

To scale and improve accuracy of impedance techniques for drug discovery applications, we integrate custom designed complementary metal-oxide-semiconductor (CMOS) integrated circuit (IC) chips[12] into each well of a standard form factor 96-well plate (Fig. 1a-c). A custom 96-well plastic (polyethylene terephthalate/PET) plate is attached via epoxy to CMOS ICs mounted on a printed circuit board in a standard form factor compatible with high-throughput instruments such as automated fluid handlers. Each well has a 140 µL maximum capacity and 120 µL working volume with a bottom diameter of 3.4 mm (Fig. 1c). A 64×64 array of 4,096 pixels at a 25 µm pitch at the bottom of the well results in a 1.6 × 1.6 mm^2 total sensing area. Each pixel contains a gold electrode[13], a digital memory, and switches to form connections with peripheral circuits (Supplementary Fig. 1). Electrochemical images with 25 µm resolution are generated across the full 96-well plate in 40 seconds. The ability for readout via USB allows 8× plates to operate simultaneously within an incubator using power and USB hubs (Fig. 1a and Supplementary Fig. 2). The real-time, live-cell impedance data is typically acquired at a frame per 5-15 minutes and fed through a cloud-based data science pipeline. Analysis includes feature extraction, high dimensional clustering, and integration with known compound metadata to identify phenotypes and relate them to cell function (Fig. 1d).

Impedance based-measurements for assessing live-cell morphology

Our plates electrically measure live cells growing over the electrode array by performing impedance measurements with two different electric field configurations[12] named vertical field

(VF) and lateral field (LF) and at four different frequencies of 250 Hz, 1 kHz, 4 kHz, and 16 kHz (Fig. 2). In total, we measure 9 impedance parameter maps per field configuration, including magnitude and phase for the 4 frequencies and a Direct Current (DC, 0 Hz) magnitude (Methods). To help explain the measurements and to demonstrate the orthogonality of the parameters, we highlight an experiment in Fig. 2 using MDCK cells, an epithelial cell line that forms a strong cell barrier and has demonstrated apical to basal water transport resulting in tissue doming or hemicysts[14–16]. We observe concrete ties between biological information and certain measurements, while the full extent of information across all frequency magnitudes, phases, and DC is still being explored.

At lower frequencies (250 Hz, 1 kHz), the capacitive nature of the cell membrane's lipid bilayer results in a very high impedance – in the VF, this causes the field to pass through intercellular spaces resulting in measurement of the permeability of the tissue or barrier. In the MDCK experiment, an increasing VF 250 Hz barrier is observed after confluency is reached reflecting the process of tight junction formation[17] and reaches a peak after the onset of water transport[18]. At higher frequencies (4 kHz, 16 kHz), the fields are sensitive to membranes in closer proximity to the electrodes. For the VF configuration, high frequency signals reflect cell size: the flatter the cell, the more cell membranes are near the electrode increasing the impedance. To this end, a spike in the VF 16 kHz is observed in the experiment shortly after plating attributed to the suspended cells falling to the surface and spreading[19].

In the high frequency LF, cell substrate attachment is measured with high sensitivity: the closer the cells are to the electrode, the higher the LF 16 kHz impedance. In the MDCK experiment, the cells reach confluence and attach strongly to the surface followed by a rapid detachment with the

onset of water transport. The water transport process can be accelerated by media changes, as in Fig. 2b, and is also affected by plating density (Supplementary Fig. 3 and Supplementary Video 1). The spatial resolution of our measurements enabled detection of doming (Fig. 2c)[14,15]; a phenomenon in which transepithelial water transport leads to areas of increased water pressure under the cell sheet. This causes the cell sheet to lift off in dome-shaped structures. In our measurements, we observe domes as circular decreases in attachment signals, represented in the bottom image of Fig. 2c as purple dots of ~150 μm diameter.

Beyond fields and frequencies, confluence can be used to parameterize cell growth/death and is calculated as the percentage area covered by cells determined using a threshold (Fig. 2a, Methods). Cell locations are also used to mask impedance maps to account for differences in confluency and to omit data from non-covered electrodes – improving accuracy beyond traditional aggregate well techniques. Finally, we use the root mean square (RMS) of the difference from one measurement frame to another for parameterizing transient features such as motility and migration (Methods), as we highlight in the next section.

Using impedance measurements to characterize a range of cell types

To test the sensitivity of our platform, we measured a wide range of well characterized cell types spanning from primary epithelial cells to cancer epithelial cells, to suspension cells (Fig. 3). The cell types originate from the kidney, brain endothelial/blood brain barrier (BBB), colon, lung, breast, and bone marrow/leukemia and are of human origin, except the MDCK cells which are canine origin. The impedance techniques measured characteristics of all cell types tested (Fig. 3a); Supplementary Fig. 3 shows real-time traces for various plating densities (typically 10,000 to

40,000 cells/well) and Supplementary Video 1 shows an example well for each density and cell type for the first 48 hours of culture growth.

The epithelial cells exhibited a strong attachment to the substrate, and many had tight cell-cell junctions that create a high barrier (Fig. 3a). Beyond MDCK, these cell types include Caco-2 (colon cancer cells that are used as a model of intestinal barrier and inflammation[20]), Calu-3 (lung adenocarcinoma cells used as a model of bronchial barrier[21]), and MCF-7 (luminal A type breast cancer cells exhibiting differentiated mammary epithelium properties[22,23]). In contrast, a variety of cell types from similar human tissue origins did not create barriers. These cell types include HT-29 and HCT116 (two types of colon cancer cells[24,25]), A549 (lung adenocarcinoma cells derived from alveoli[26]), and MDA-MB-231 (triple negative breast cancer cells that have undergone EMT[27]). To complement the cancer cells, hCMEC/D3 (brain endothelial cells used for modeling BBB function[28]) exhibited the highest motility of any cell type (see also Supplementary Video 1). Finally, K-562 (suspension cells from CML patients) were effectively measured and the presence of live cells above the electrodes could be readily identified. As expected, suspension cells had the lowest cell attachment signal of all the tested cell lines.

We performed immunofluorescence imaging for representative cell types to detect expression and localization of E-cadherin, a functional component of adherens junctions expressed in normal epithelia, and compared the results to impedance images (Fig. 3b). Loss of E-cadherin can cause dedifferentiation and invasiveness in human carcinomas and is observed in cancer cells that have undergone EMT[29]. We observe that cell types with high-levels of membrane E-cadherin and a regular epithelial morphology (MDCK, Caco-2, and MCF-7) have a correspondingly high barrier signal (Fig. 3b left panel). In contrast, cells with low/diffused (A549) or undetectable levels

(MDA-MB-231) of E-cadherin do not exhibit a barrier signal, consistent with the previous literature (Fig. 3b left panel). Different impedance image textures were also observed for the no-barrier cell types: the A549 cells optically have an epithelial morphology and measure with a smoother impedance texture than the MDA-MB-231 cells which have a mesenchymal morphology and have a more dynamic and rougher texture (Fig. 3b right panel and Supplementary Video 1).

Within the body, epithelial cells grow within extracellular matrix (ECM) – integrin signaling through the ECM is an important regulator of epithelial cell polarity and morphogenesis[30]. To this end, we tested the compatibility of coatings in our platform by plating Caco-2 cells in wells with or without a collagen type I coating (Fig. 3c). Cells grown on collagen were successfully measured and had a lower attachment signal reflecting the increased distance of the cells from the electrode (e.g., the LF measurement schematic of Fig. 2a), highlighting the sensitivity of our technique. To further test the limits of sensitivity, we performed an experiment studying breast cancer cells exhibiting distinct phenotypes, co-cultured in different ratios (Fig. 3d). As observed in Fig. 3a-b, MCF-7 shows an epithelial morphology and expression of E-cadherin while MDA-MB-231 shows a mesenchymal phenotype with no expression of E-Cadherin. Graded responses corresponding to the ratio of the two breast cancer cell types were observed in the cell size parameter (VF 16 kHz) and movement (RMS) across the mixtures, allowing quantification of the overall epithelial versus mesenchymal phenotype of the mixed populations.

Real-time compound effects measured across epithelial to mesenchymal cell types

Having established our platform's sensitivity to measure inherent differences in cell morphology and function, we performed compound screening to help reveal the range of functional phenotypes that can be observed. Two approaches were taken. In the first, we chose three cell types

representing a range of characteristics, MDCK, A549, and MDA-MB-231, and applied a common set of compounds that target various cellular processes; line traces are shown in Supplementary Figs. 4-6 and full well-plate videos in Supplementary Videos 2-4. The compounds chosen (Cytochalasin D, Vinblastine Sulfate, Paclitaxel, Alisertib, Bosutinib, Anisomycin, Dexamethasone, Getfitinib, Decitabine, Cyclophosphamide Monohydrate, and GSK 269962A) target various cellular processes including cell division, DNA replication, inflammation and various other signaling pathways. We studied the effect of the compounds on measurements that link to a specific biological parameter. Many diverse changes were observed and matched known effects of the compounds – increases/decreases in attachment, barrier, cell size, motility, and confluency – with differences in response across cell lines; an extended presentation of these experiments is in Supplemental Results 1.

Of particular interest was an observation that compound treatments modulating water transport properties in MDCK correlated to *in vivo* results for autosomal dominant polycystic kidney disease (ADPKD). In humans, ADPKD is thought to be caused by a combination of overgrowth of cells and a switch from an absorptive to secretive epithelium, both leading to fluid accumulation in cysts[31] which increases kidney size while decreasing kidney function[32]. In our MDCK drug treatments, we found that Alisertib, an Aurora kinase inhibitor, accelerated transepithelial water transport as evidenced by a sharp decrease in cell surface attachment and increased doming (Fig. 4 and Supplementary Video 2). In contrast, Bosutinib, a multi-kinase inhibitor, decelerated water transport as evidenced by a slower decrease of cell attachment and no domes. Interestingly, Alisertib has been shown to exacerbate ADPKD in animal models[33] while Bosutinib was in Phase II clinical trials for treatment of ADPKD[34], matching the differential signatures of the MDCK experiment.

Mechanism of action (MOA) identification using high-dimensional impedance measurements

In our second approach, rather than comparing 5 measurement parameters, we used all field and calculation parameters to perform an unbiased phenotypic profiling with a larger compound library. We chose 341 compounds as a sub-set of an FDA approved library and applied them on two cell types, A549 and Caco-2. At least two compounds per target were chosen for conserved phenotype effects. For the screens, compounds were added 24 or 48 hours post cell seeding and measured up to 48 hours after the compound addition (see Methods for an extended description). Time normalization, a principal component analysis (PCA), and unbiased clustering were sequentially performed on the high-dimensional data readouts (VF & LF magnitudes, phase, and DC). This unbiased approach ensures compound separation based solely on functional and morphological effects of the cells, with no bias of the targets/pathways of the compounds. Positive controls across the plates helped assess the variance in the data and validated our clustering; Anisomycin was chosen as a positive control for the A549 (separated into its own cluster in Fig. 5) as it shows increases in VF across many cell types (Supplementary Figs. 2-4) while Anisomycin, Bosutinib, and YM-201636 were used as positive controls for the Caco-2 (separated into unique clusters in Supplementary Fig. 7). We present a subset of the phenotypes measured from the A549 screen in Fig. 5 and the Caco-2 in Supplementary Fig. 7.

A549 has been shown to be an effective cell model for high-content phenotypic screening[35]. In our work, the A549 clustering analysis revealed interesting insights about MOA of various compounds and their effects on live-cell function. We identified a cluster consisting of several anti-inflammatory compounds (Fig. 5c) which separated in the PCA due to an increase in cell-cell

adhesion (Fig 5b, red). This cluster contains two forms of Dexamethasone which has been described to reduce inflammation and increase the tissue barrier in A549 cells[36], (Supplementary Fig. 5), corresponding with our measured MOA signature. Multiple clusters were related to cell death or growth inhibition. The end-point effects of these compounds on growth were often very similar, however, distinct transient effects on cell morphology separated compounds into different clusters. These were reflective of the MOA of the compounds in that cluster. For example, a microtubule polymerization inhibitor cluster and anti-viral cluster exhibited a similar reduction of confluency (-20% over the 48 hours), yet they separate due to distinct differences in the other parameters such as attachment and movement. In an extended analysis (Supplementary Figs. 8-9), additional clusters identifying DNA replication inhibitors, microtubule depolymerization inhibitors, antimetabolites, anti-proliferation, and reversible/irreversible proteasome inhibitors separate as distinct clusters based on their transient morphological effects. Thus, our platform is sensitive enough to separate very closely related compounds based on their effects on cell state.

Some compounds clustered by target. For example, most Akt/mTOR inhibitors[37] had a similar effect on cell function. Interestingly, while these compounds have relatively minor effects on many morphological properties of cells, it is one of the few clusters that causes an increase in movement (RMS); an additional Akt/mTOR cluster is shown in Supplementary Fig. 10. In another example, a common annotated function was not evident, such as the anti-viral cluster containing compounds that target NF-KB, DNA synthesis and STAT. However, upon deeper investigation, all the compounds in the cluster were identified as functional hits during an anti-viral phenotypic screen for SARS-CoV-2[38] suggesting common underlying function.

Barrier function screen on Caco-2 gut model identifies new MOA for tightening junctions

Caco-2 cells are widely used to model intestinal epithelia barrier function and study modulators of tight junction in epithelia[20,39]. Our Caco-2 screen identified Amonafide, a DNA intercalating agent and Topoisomerase II inhibitor, and Ciclopirox, an antifungal iron chelator, as compounds that cause the largest barrier increase over the 48-hours (Fig. 6a); a subsequent dose response experiment confirmed the screen hits (Fig. 6b). Amonafide caused a rapid increase in barrier suggesting modulation through cell signaling or protein changes, while Ciclopirox caused a more gradual increase in barrier, suggesting longer term responses such as change in gene expression. To further investigate the specificity and test the observed rapid response, we acquired commercially available analogues of Amonafide (Fig. 5c) and measured their effects on Caco-2 barrier (Fig. 5d and Supplementary Fig. 11). Only one of the derivatives, NSC 308848, showed a similar increase in barrier. Interestingly, UNBS5162, a structurally similar compound that retains the DNA intercalation activity does not affect the barrier. Similarly, Etoposide, a Topoisomerase II inhibitor that does not intercalate DNA also did not show the rapid barrier increase. This points to the observed increase in barrier being non-random, and potentially independent of both its DNA intercalation and Topoisomerase inhibitor activity. To explore whether the increase in barrier was also reflected in changes at tight junctions, we performed immunofluorescence imaging to look at tight junction proteins ZO-1 and Occludin (Fig. 6e). Amonafide treatment led to an increase in membrane ZO-1 levels, with additional nuclear localization (Fig. 6e ZO-1 quantification in Supplementary Fig. 12). NSC 308848 had a similar effect on ZO-1 expression, while UNBS5162, that did not show the barrier increase, did not affect ZO-1 levels or distribution. This suggests that the change in ZO-1 is directly related to the observed increase in barrier. Interestingly, although Ciclopirox increases the barrier, it did not affect ZO-1 distribution or expression and likely tightens

barriers through a different mechanism. Therefore, our real-time data was able to identify two different MOAs of barrier tightening, that were further validated by our immunofluorescence data.

ZO-1 has been shown to relocate to the nucleus during remodeling of tight junctions and its nuclear vs. membrane localization is related to cell-signaling[40]. Taken together, the rapid and sustained increase in the measured barrier of the Caco-2 sheet with the increase in ZO-1 expression and localization towards the nucleus, strongly suggests a direct effect of Amonafide on tight junctions, potentially through activating signaling pathways. Furthermore, the similar response measured for NSC 208848 and not UNBS5162 or Etoposide, suggests an off-target MOA other than its primary pharmacological action as an intercalating agent and Topoisomerase II inhibitor.

Discussion

Consumer electronic CMOS devices have demonstrated electrochemical measurement of live-cells, but traditional single-well form factors have prevented high-throughput applications[12]. Some notable deviations are Maxwell Biosystems AG[41] and 3Brain AG[42] which sell 24- and 96-well CMOS-based plates for neural applications. Our work is differentiated in two ways. First, by both forming the CMOS electronic 96-microplates and miniaturizing interfacing off-plate electronics, we perform multiple plate operation directly in the incubator, enabling high throughput applications (Fig. 1). Our current set-up measures 8 plates in parallel, but in principle, can be easily scaled to 10s or 100s of plates through improved USB and power hub interfaces. Second, we demonstrate novel impedance techniques capable of measuring a wide range of cell biology (Fig. 2-6). These cell-type agnostic capabilities open application areas beyond neuroscience, such as cancer and epithelial disease screening.

Another important aspect for high throughput drug discovery is data reproducibility and scalability. We found high repeatability of cell impedance parameters on our platform: summary statistics for the two presented screens and additional experiments show consistent results before compound additions (Supplementary Fig. 12). Furthermore, we found that the real-time capability allowed removal of wells with outlier characteristics before compound treatment, ensuring a reliable and repeatable starting phenotypic state[35]. Such pre-drug assessment is not possible with end-point assays, including high-content imaging which requires cell fixing.

The combination of multiple field and frequency impedance parameters helps generate a label-free, high-dimensional electrical representation of cell state, based in part on morphology and cell function. Real-time readouts then allow state changes to be observed over time. This generates a wealth of information on the intermediate cell states in a drug response. Determining cell death MOAs is a ready application for these capabilities: as cell death is innately a physical process, our platform is highly sensitive to the morphology of cell death and its 'order of operations'[43] (examples in Supplementary Fig. 8 from the A549 screen). This label-free, MOA profiling capability could find wide-use throughput *in vitro* toxicology, which heavily relies upon end-point readouts that are blind to cell state transitions and potential off-target activities[44]. Of note, our current analysis uses a subset of the time points measured and does not fully use spatial data in the analysis. Transient and spatial feature extraction using more advanced computational techniques[2] will likely increase our ability to differentiate between compound effects.

To complement the breadth of information for MOA assessment, many of our functional parameters cannot currently be measured accurately nor at scale by another technology. Thus, our platform can enable novel therapeutic approaches in many disease areas. For example, our

technology is the only functional readout for water transport. The strong correlation of the compound responses on the water transport phenotype of MDCK cells (Fig. 4 and Supplementary Video 2) and ADPKD animal and human studies provides avenues for ADPKD screening applications[7]. Beyond the kidney, doming as evidence of water transport is observed in other cell types, including Caco-2 and Calu-3 (Supplementary Fig. 13). These additional cell types could create effective phenotypic models for other diseases, such as chronic diarrhea or cystic fibrosis. The water transport phenotype is also of great interest in functional aquaporin inhibitor screening, an untouched drug discovery area spanning oedema, cancer, obesity, brain injury, glaucoma, and other conditions[45], that is blocked in part due to a lack of a reliable assay[46].

Epithelial leakiness, or barrier dysfunction[5], occurs from physical damage or modifications to tight junctions and is important in the context of inflammatory bowel disease (IBD), celiac disease, Crohn's disease, and other diseases of the gut[47–50]. Most therapeutic approaches to IBD have focused on anti-inflammatory or immune-suppressive therapies[51,52] but more recently, direct tightening of the epithelial barrier is being explored as a therapeutic approach[53,54]. Our screen using Caco-2 cells revealed a potentially new MOA for increasing barrier and demonstrates the power of screening against physiologically relevant parameters in higher throughputs. Amonafide has inherent toxicity and is not a good therapeutic candidate for IBD as a result. However, our study of analogues demonstrates that our platform has the sensitivity for an in-depth medicinal chemistry, structure activity relationship (SAR) approach for developing lead compounds. The expansion of compounds screened could also help identify additional modulators of intestinal barrier as potential therapeutic molecules.

Online Methods

Impedance measurements

To accomplish the field-based impedance measurements across multiple frequencies, we apply a voltage stimulation which is the summation of the four different frequency signals and measure return currents using a transimpedance amplifier (TIA) with a feedback gain of 18 MΩ[12]. The magnitudes of the AC voltage signals are scaled to create similar output amplitudes that are measured by the TIA (0.2 V/250 Hz, 0.08 V/1 kHz, 0.04 V/4 kHz, and 0.02 V/16 kHz for lateral field, 0.25 V/250 Hz, 0.1 V/1 kHz, 0.04 V/4 kHz, and 0.025 V/16 kHz for vertical field). Six of the 96 wells are scanned at a time taking 2.5 s, resulting in a total scan time across the well plate of 40 s. A fast Fourier transform (FFT) is used to extract the magnitude and phase of each of the four frequencies and the DC component – 9 impedance parameter maps for each field configuration. We observe that different frequencies contain different types of biological information (highlighted in Fig. 2) but are still biologically understanding the extant of information captured across the magnitude, phase, and DC information.

Cell location masking and root-mean-square (RMS) calculation

A reference impedance map is used to determine the location of cells: a threshold is set above the electrodes' default impedance in solution, the presence of a cell above an electrode then increases the impedance beyond the threshold for detection. Typically, the VF 4 kHz map provides the best contrast for generating the cell mask. For magnitude, phase, and DC, the median value of pixels with cells is then calculated. Additional metrics of the well distributions are being explored (e.g. standard deviation, 10%/90% distribution markers) but are not reported in this work. An additional

epoxy mask is calculated in a similar manner to remove pixels which have spillover epoxy from the plastic well plate attachment, see example in Supplementary Video 4. Before each cell plating, a reference measurement is taken in empty culture media to calculate the epoxy mask.

Transient features such as motility and migration are generated from the impedance videos through a root-mean-square (RMS) calculation. The difference between two unmasked image frames is taken (the epoxy mask is still used if applicable), then the RMS calculation is performed across the pixels of the difference map. To normalize for changes in magnitude, the calculated RMS is then divided by the median value of the cell-masked well distribution. Typically, the VF 4 kHz map is used for the RMS signal generation, and is used throughout this paper for Figs. 2, 3, and 5.

Proof of concept screens and data-analysis

To execute and analyze the screens, we seeded cells on five CMOS 96-wellplates, let them grow for 24 hours for A549 or 48 hours for Caco-2, added compounds at 10 μM in 1% DMSO via a half media swap using an OpenTrons liquid handling robot, and measured effects for 48 hours; impedance measurements were taken every 15 minutes. The many field/frequency and calculated parameters were then normalized to a timepoint one hour before compound addition. The array of normalized parameters at timepoints logarithmically spaced from compound addition to +48 hours were then used for a principal component analysis (PCA) and unbiased clustering using the top 20 PCA dimensions – we found the logarithmic time spacing balanced rapid binding effects and longer-term effects increasing/decreasing over the full 48 hours.

1 **Cell culture and seeding**

2 All cell lines were obtained from ATCC and maintained in a humidified incubator at 37 C and 5%
3 CO2 . MCF-7, A549, MDA-MB-231, MDCK, Calu-3 and HCT116 cells were cultured in DMEM
4 supplemented with 10% FBS. Caco-2 cells were cultures in EMEM supplemented with 20% FBS.
5 K-562 cells were cultures in IMDM supplemented with 10% FBS. HT-29 cells were cultured in
6 McCoy's 5A medium supplemented with 10% FBS. hCMEC/D3 cells were cultured in EndoGRO
7 media obtained from Millipore.

8 Cell lines were seeded in the semiconductor 96-miroplates at various densities as indicated.
9 Collagen-1 – rat tail was obtained from Corning, and plates were coated according to
10 manufacturer's instructions. All measurements both pre and post compound treatment were
11 performed in an incubator regulating CO_2, humidity, and temperature.

12 **Immunofluorescence**

13 For immunofluorescence imaging, cells were grown on coverslips and then either allowed to grow
14 for 48 hours or treated with relevant compounds for 48 hours. Cells were then fixed in 4%
15 paraformaldehyde, washed, permeabilized with 0.5% Triton-X 100 in PBS, and then subjected to
16 antibody incubation. Antibodies used were anti-E-Cadherin (Cell Signaling Technology Cat no:
17 3195T), anti-ZO1(Thermo Fisher, Cat no:617300) and anti-Occludin (Thermo Fisher, Cat
18 no:331500). Alexa Fluor 488 and 568 secondary antibodies were used. Coverslips were mounted
19 in Vectashield antifade mounting medium with DAPI.

Imaging and image analysis

Imaging was performed using a Yokogawa W1 spinning disk confocal on an inverted Nikon Ti fluorescence microscope equipped with Hamamatsu ORCA-Fusion BT CMOS camera (6.5 µm2 photodiode) , Lumencor SOLA fluorescence light source , and Nikon LUN-F XL solid state laser combiner: 405 (80mW), 445 (35mW), 488 (80mW), 514 (50mW), 561 (65mW), 640nm (60mW). For imaging we mainly used the widefield modality of the microscope and all imaging were done using 20X objective. Acquisition was done using consistent exposure across samples, to enable intensity quantification. Images were processed for publication using FIJI, open source image processing software.

Quantification of ZO-1 in the cell-membrane and nucleus, was performed by manually defining ROIs for the cell membrane and nucleus. Mean integrated intensity was calculated within the ROI All quantification was performed in raw, unprocessed images.

Compound treatments

Compound treatments were performed using a half media exchange. To prepare for compound addition, half the media from each well of 96-well plate was removed. Compounds were prepared at 2× concentration in cell culture media, the 2× compound solution was then added to the wells. Care was taken to keep DMSO concentration below 1%, compound dilutions were performed with a constant DMSO concentration. Compound in media was temperature and CO_2 equilibrated prior to addition. All compounds including the 341 compound library were obtained from Selleckchem Chemicals. For the screening analysis, the pathway and target information provided by Selleckchem Chemicals was curated together.

Author Contributions

J.A., H.P., D.H., M.B., D.S., A.M., W.W., and S.C. conceived and designed the experiments. W.W., H.H., and J.A. designed the CMOS integrated circuit, W.W., M.C., Z.B., A.A., and J.A. designed the electronic platform, H.M., B.P., and H.W. designed the software environment, S.C., W.W., A.M., H.L., P.S., I.N., C.A., R.S.G., and J.A. performed the experiments, M.B., D.H., H.P., and J.A. supervised the collaborative project. S.C. and J.A. wrote the manuscript, and all authors read and discussed it.

Conflicts of interest

W.W. and J.A. contributed to the work at Harvard University and transitioned to employment at CytoTronics. S.C., H.L., P.S., I.N., C.A., H.M., B.P., H.W., M.C., Z.B., A.A., and D.S. were employed at CytoTronics during their contributions to the work. D.H. and H.P. hold shares in CytoTronics. D.H. is also a Fellow of Samsung Electronics, but there is no competing interest for this work D.H. performed exclusively at Harvard University. The other authors declare that there are no conflicts of interest.

Acknowledgements

The authors are grateful for the support of this research by Samsung Advanced Institute of Technology, Samsung Electronics, Suwon, Republic of Korea (A37734 to D.H. and A37738 to H.P.), the Army Research Office (W911NF-15-1-0565 to D.H.), the Army Research Office (W911NF-17-1-0425 to D.H.), and the Gordon and Betty Moore Foundation (to H.P.). M.B. was supported by Maximizing Investigators' Research Award (5R35GM137895) and the Harvard Medical School Junior Faculty Armenise grant.

References

1. Chandrasekaran, S. N., Ceulemans, H., Boyd, J. D. & Carpenter, A. E. Image-based profiling for drug discovery: due for a machine-learning upgrade? *Nat Rev Drug Discov* **20**, 145–159 (2021).

2. Bray, M.-A. *et al.* Cell Painting, a high-content image-based assay for morphological profiling using multiplexed fluorescent dyes. *Nat Protoc* **11**, 1757–1774 (2016).

3. Janiszewska, M., Primi, M. C. & Izard, T. Cell adhesion in cancer: Beyond the migration of single cells. *Journal of Biological Chemistry* **295**, 2495–2505 (2020).

4. Tschumperlin, D. J., Ligresti, G., Hilscher, M. B. & Shah, V. H. Mechanosensing and fibrosis. *Journal of Clinical Investigation* **128**, 74–84 (2018).

5. Buckley, A. & Turner, J. R. Cell Biology of Tight Junction Barrier Regulation and Mucosal Disease. *Cold Spring Harb Perspect Biol* **10**, a029314 (2018).

6. Turcios, N. L. Cystic Fibrosis Lung Disease: An Overview. *Respir Care* **65**, 233–251 (2020).

7. Olesen, E. T. B. & Fenton, R. A. Aquaporin 2 regulation: implications for water balance and polycystic kidney diseases. *Nat Rev Nephrol* **17**, 765–781 (2021).

8. Xu, Y. *et al.* A review of impedance measurements of whole cells. *Biosens Bioelectron* **77**, 824–836 (2016).

9. Srinivasan, B. *et al.* TEER Measurement Techniques for In Vitro Barrier Model Systems. *J Lab Autom* **20**, 107–126 (2015).

10. Ke, N., Wang, X., Xu, X. & Abassi, Y. A. The xCELLigence system for real-time and label-free monitoring of cell viability. *Methods Mol Biol* **740**, 33–43 (2011).

11. Wegener, J., Keese, C. R. & Giaever, I. Electric cell-substrate impedance sensing (ECIS) as a noninvasive means to monitor the kinetics of cell spreading to artificial surfaces. *Exp Cell Res* **259**, 158–166 (2000).

12. Abbott, J. *et al.* Multi-parametric functional imaging of cell cultures and tissues with a CMOS microelectrode array. *Lab Chip* **22**, 1286–1296 (2022).

13. Park, J. S. *et al.* Multi-parametric cell profiling with a CMOS quad-modality cellular interfacing array for label-free fully automated drug screening. *Lab Chip* **18**, 3037–3050 (2018).

14. Valentich, J. D., Tchao, R. & Leighton, J. Hemicyst formation stimulated by cyclic AMP in dog kidney cell line MDCK. *J Cell Physiol* **100**, 291–304 (1979).

15. Latorre, E. *et al.* Active superelasticity in three-dimensional epithelia of controlled shape. *Nature* **563**, 203–208 (2018).

16. Ramírez-Rodríguez, G., Meza, I., Hernández, M. E., Castillo, A. & Benítez-King, G. Melatonin induced cyclic modulation of vectorial water transport in kidney-derived MDCK cells. *Kidney Int* **63**, 1356–1364 (2003).

1 17. Gonzalez-Mariscal, L., Chávez de Ramírez, B. & Cereijido, M. Tight junction formation in
2 cultured epithelial cells (MDCK). *J Membr Biol* **86**, 113–125 (1985).

3 18. Shigetomi, K., Ono, Y., Inai, T. & Ikenouchi, J. Adherens junctions influence tight junction
4 formation via changes in membrane lipid composition. *Journal of Cell Biology* **217**, 2373–
5 2381 (2018).

6 19. Cuvelier, D. *et al.* The Universal Dynamics of Cell Spreading. *Current Biology* **17**, 694–
7 699 (2007).

8 20. Sambuy, Y. *et al.* The Caco-2 cell line as a model of the intestinal barrier: influence of cell
9 and culture-related factors on Caco-2 cell functional characteristics. *Cell Biol Toxicol* **21**,
10 1–26 (2005).

11 21. Foster, K. A., Avery, M. L., Yazdanian, M. & Audus, K. L. Characterization of the Calu-3
12 cell line as a tool to screen pulmonary drug delivery. *Int J Pharm* **208**, 1–11 (2000).

13 22. Martin, T. A., Das, T., Mansel, R. E. & Jiang, W. G. Enhanced tight junction function in
14 human breast cancer cells by antioxidant, selenium and polyunsaturated lipid. *J Cell*
15 *Biochem* **101**, 155–166 (2007).

16 23. Vantangoli, M. M., Madnick, S. J., Huse, S. M., Weston, P. & Boekelheide, K. MCF-7
17 Human Breast Cancer Cells Form Differentiated Microtissues in Scaffold-Free Hydrogels.
18 *PLoS One* **10**, e0135426 (2015).

24. Rajput, A. *et al.* Characterization of HCT116 Human Colon Cancer Cells in an Orthotopic Model. *Journal of Surgical Research* **147**, 276–281 (2008).

25. Hekmati, M., Ben-Shaul, Y. & Polak-Charcon, S. A morphological study of a human adenocarcinoma cell line (HT29) differentiating in culture. Similarities to intestinal embryonic development. *Cell Differentiation and Development* **31**, 207–218 (1990).

26. Garcia-de-Alba, C. Repurposing A549 Adenocarcinoma Cells: New Options for Drug Discovery. *Am J Respir Cell Mol Biol* **64**, 405–406 (2021).

27. Cailleau, R., Young, R., Olive, M. & Reeves, W. J. *Breast Tumor Cell Lines From Pleural Effusions 1,2*. *JOURNAL OF THE NATIONAL CANCER INSTITUTE* vol. 53 (1974).

28. Weksler, B., Romero, I. A. & Couraud, P. O. The hCMEC/D3 cell line as a model of the human blood brain barrier. *Fluids Barriers CNS* **10**, 1–10 (2013).

29. Pećina-Šlaus, N. Tumor suppressor gene E-cadherin and its role in normal and malignant cells. *Cancer Cell Int* **3**, 17 (2003).

30. Manninen, A. Epithelial polarity – Generating and integrating signals from the ECM with integrins. *Exp Cell Res* **334**, 337–349 (2015).

31. Choudhury, M. I. *et al.* Kidney epithelial cells are active mechano-biological fluid pumps. *Nat Commun* **13**, 2317 (2022).

32. Bergmann, C. *et al.* Polycystic kidney disease. *Nature Reviews Disease Primers 2018 4:1* **4**, 1–24 (2018).

1 33. Nikonova, A. S. *et al.* Opposing Effects of Inhibitors of Aurora-A and EGFR in Autosomal-
2 Dominant Polycystic Kidney Disease. *Front Oncol* **5**, (2015).

3 34. Tesar, V. *et al.* Bosutinib versus Placebo for Autosomal Dominant Polycystic Kidney
4 Disease. *Journal of the American Society of Nephrology* **28**, 3404–3413 (2017).

5 35. Heinrich, L., Kumbier, K., Li, L., Altschuler, S. J. & Wu, L. F. Selection of Optimal Cell
6 Lines for High-Content Phenotypic Screening. *ACS Chem Biol* (2023)
7 doi:10.1021/acschembio.2c00878.

8 36. Hermanns, M. I., Unger, R. E., Kehe, K., Peters, K. & Kirkpatrick, C. J. Lung epithelial cell
9 lines in coculture with human pulmonary microvascular endothelial cells: development of
10 an alveolo-capillary barrier in vitro. *Laboratory Investigation* **84**, 736–752 (2004).

11 37. Alzahrani, A. S. PI3K/Akt/mTOR inhibitors in cancer: At the bench and bedside. *Semin*
12 *Cancer Biol* **59**, 125–132 (2019).

13 38. Chen, Y. *et al.* A high-throughput screen for TMPRSS2 expression identifies FDA-
14 approved compounds that can limit SARS-CoV-2 entry. *Nat Commun* **12**, (2021).

15 39. Balimane, P. V. & Chong, S. Cell culture-based models for intestinal permeability: A
16 critique. *Drug Discov Today* **10**, 335–343 (2005).

17 40. Gottardi, C. J., Arpin, M., Fanning, A. S. & Louvard, D. The junction-associated protein,
18 zonula occludens-1, localizes to the nucleus before the maturation and during the

remodeling of cell-cell contacts. *Proceedings of the National Academy of Sciences* **93**, 10779–10784 (1996).

41. Müller, J. *et al.* High-resolution CMOS MEA platform to study neurons at subcellular, cellular, and network levels. *Lab Chip* **15**, 2767–2780 (2015).

42. Seu, G. Pietro *et al.* Exploiting All Programmable SoCs in Neural Signal Analysis: A Closed-Loop Control for Large-Scale CMOS Multielectrode Arrays. *IEEE Trans Biomed Circuits Syst* **12**, 839–850 (2018).

43. Galluzzi, L. *et al.* Molecular mechanisms of cell death: recommendations of the Nomenclature Committee on Cell Death 2018. *Cell Death Differ* **25**, 486–541 (2018).

44. Pognan, F. *et al.* The evolving role of investigative toxicology in the pharmaceutical industry. *Nat Rev Drug Discov* (2023) doi:10.1038/s41573-022-00633-x.

45. Verkman, A. S., Anderson, M. O. & Papadopoulos, M. C. Aquaporins: important but elusive drug targets. *Nat Rev Drug Discov* **13**, 259–277 (2014).

46. Salman, M. M., Kitchen, P., Yool, A. J. & Bill, R. M. Recent breakthroughs and future directions in drugging aquaporins. *Trends Pharmacol Sci* **43**, 30–42 (2022).

47. Xavier, R. J. & Podolsky, D. K. Unravelling the pathogenesis of inflammatory bowel disease. *Nature* **448**, 427–434 (2007).

48. Guan, Q. A Comprehensive Review and Update on the Pathogenesis of Inflammatory Bowel Disease. *J Immunol Res* **2019**, 1–16 (2019).

49. Michielan, A. & D'Incà, R. Intestinal Permeability in Inflammatory Bowel Disease: Pathogenesis, Clinical Evaluation, and Therapy of Leaky Gut. *Mediators Inflamm* **2015**, 1–10 (2015).

50. Martel, J. *et al.* Gut barrier disruption and chronic disease. *Trends in Endocrinology & Metabolism* **33**, 247–265 (2022).

51. Furfaro, F., Ragaini, E., Peyrin-Biroulet, L. & Danese, S. Novel Therapies and Approaches to Inflammatory Bowel Disease (IBD). *J Clin Med* **11**, 4374 (2022).

52. Laukoetter, M. G., Nava, P. & Nusrat, A. Role of the intestinal barrier in inflammatory bowel disease. *World J Gastroenterol* **14**, 401 (2008).

53. Odenwald, M. A. & Turner, J. R. The intestinal epithelial barrier: A therapeutic target? *Nat Rev Gastroenterol Hepatol* **14**, 9–21 (2017).

54. Al-Sadi, R. *et al.* Lactobacillus acidophilus Induces a Strain-specific and Toll-Like Receptor 2–Dependent Enhancement of Intestinal Epithelial Tight Junction Barrier and Protection Against Intestinal Inflammation. *Am J Pathol* **191**, 872–884 (2021).

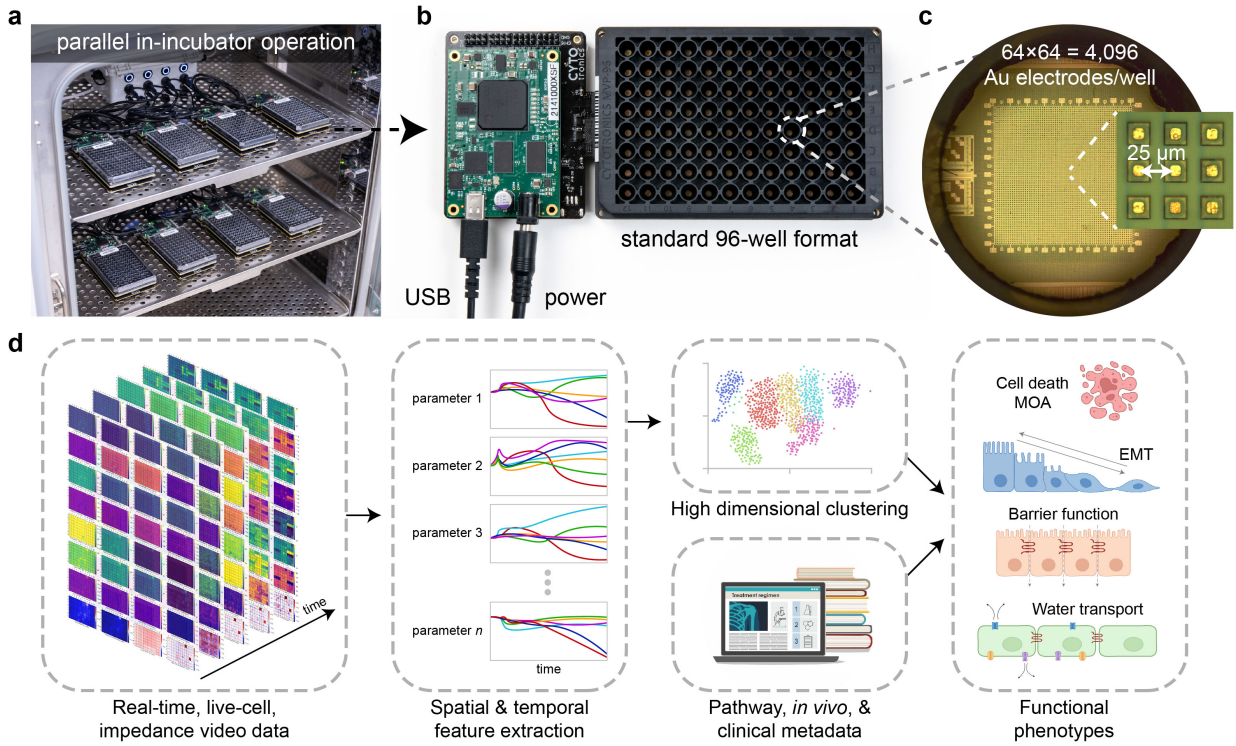

Fig. 1 | A semiconductor 96-microplate platform for in-incubator, electrochemical high-throughput screening. a, Up to 8× complementary metal-oxide-semiconductor (CMOS) microplates operate in a cell-culture incubator for high-throughput electrochemical screening. The incubator regulates the ambient temperature, CO_2, and humidity. A universal serial bus (USB) and power hub connect the microplates to an external computer. **b**, Each CMOS microplate contains 96 wells and connects to a miniaturized data acquisition system which forms a USB interface and provides power. The microplate is designed with standard dimensions so that it is compatible with wet-lab automation (e.g. automated fluid pipettes) and other instruments (e.g. centrifuge, plate reader). **c**, At the bottom of each well is a CMOS integrated circuit (IC) containing an array of 64×64 = 4,096 Au electrodes, spaced at a pitch of 25 µm. Embedded circuits scan electrochemical measurements across the array generating impedance images every 5-15 mins. **d**, For high-throughput screening applications, the real-time, live-cell, impedance videos are fed through a data science pipeline and combined with known compound metadata to identify functional phenotypes.

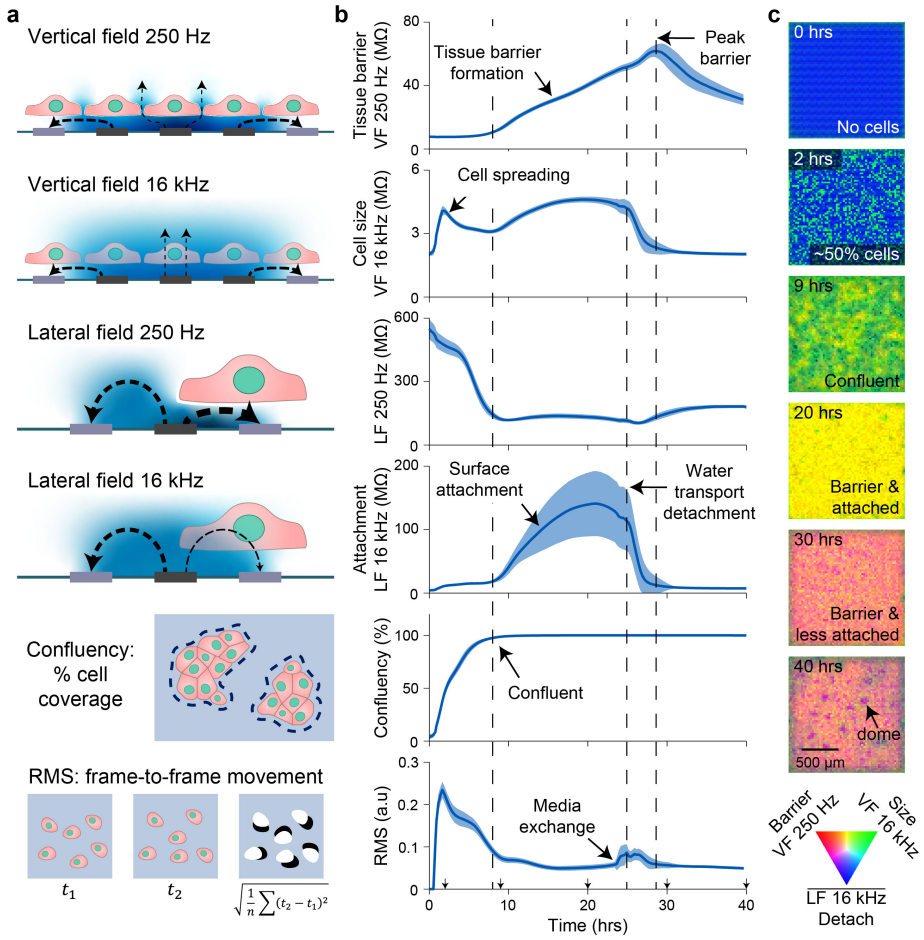

Fig. 2 | Real-time, label-free field-based impedance measurements for live-cell functional morphology measurement. a, Schematics for the vertical field (VF) and lateral field (LF) configurations, confluency, and root mean square (RMS). Examples of measured electric field lines are shown between stimulation (dark gray) and return electrodes (light gray) and potential distribution in blue. At low-frequency (250 Hz), cell membranes block the electric fields whereas at higher frequency (16 kHz) the fields become more proximately sensitive. Confluency and RMS are calculated from the impedance images. **b**, Parameter traces are shown for MDCK cells (canine kidney) plated on a 96-well CMOS microplate. Cells were seeded at time $t = 0$ hrs at a density of 40,000 cells/well and measured for 40 hrs. Media was changed at 24 hrs post seeding. The traces

represent mean ± s.d. for 88 wells across the plate. The most representative biological parameter is labeled for each measurement, but a blend of biological parameters contributes to each measurement in total. **c**. Impedance images of the MDCK cells from a single well at the indicated time points. The images were generated with VF 250 Hz in red, VF 16 kHz in green, and the inverse of the LF 16 kHz in blue.

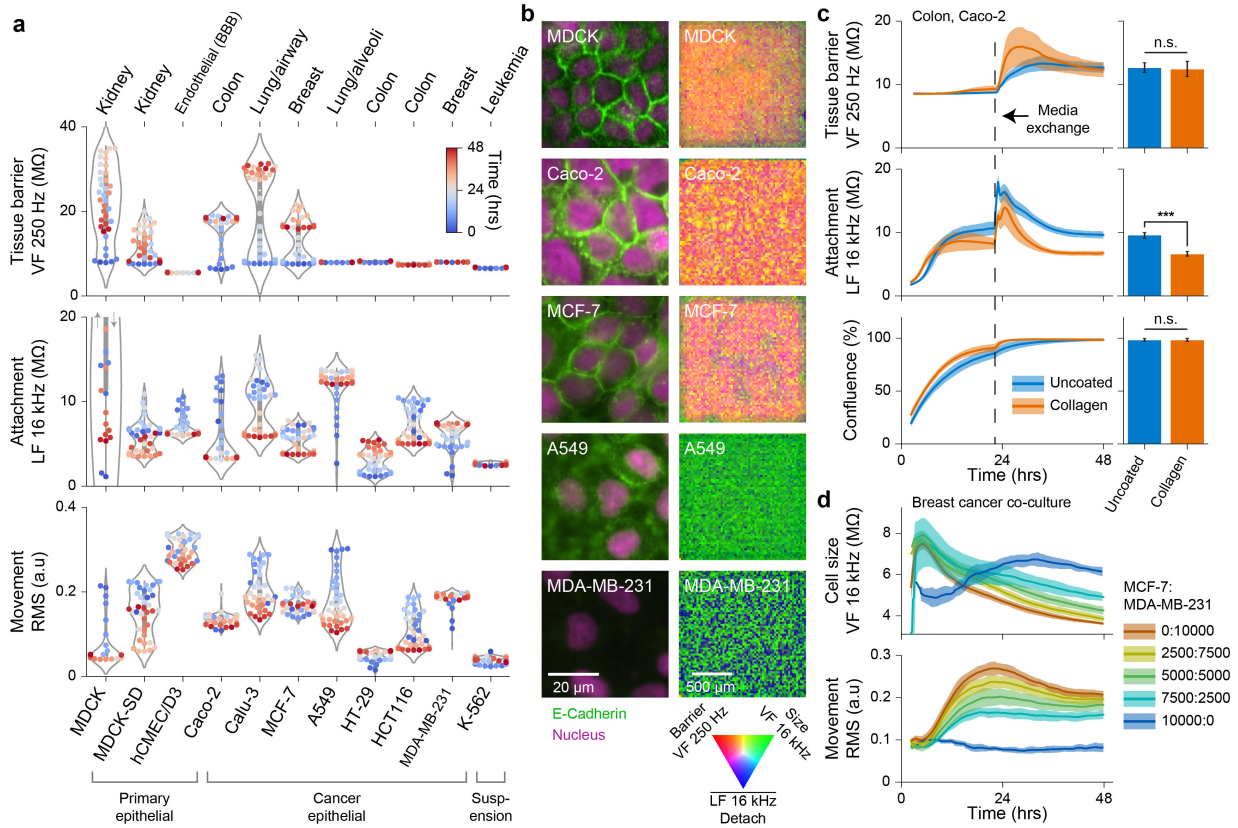

Fig. 3 | Impedance measurements differentiate a wide variety of cell types and characterize cell state over time. a, Eleven cell types were characterized using live-cell impedance measurements. Tissue origins are labeled; MDCK variants are canine, the remainder are human. Violin plots of three parameters show differences in tissue barrier (VF 250 Hz), cell-substrate attachment (LF 16 kHz), and movement/dynamic changes in morphology (RMS). Real-time videos for all cell types at different seeding densities are shown in Supplementary Video 1. **b**, Immunofluorescence images (left) and impedance images (right) for various cell types show a range of epithelial tissue properties. Cells were stained for E-Cadherin (green), a cell-cell adhesion protein, and for DAPI/nucleus (red). A representative well impedance image combines several impedance parameters into different colors (noted). Cells strongly expressing E-Cadherin at cell-cell interfaces (MDCK, Caco-2, MCF-7) show high tissue barrier in comparison to cells with

dispersed E-Cadherin (A549) or no expression (MDA-MB-231). **c**. A surface coating comparison study shows a difference in Caco-2 cell function from 0 - 48 hours after seeding. Tissues on coated surfaces increased in tissue barrier (VF 250 Hz) more significantly with a media exchange and showed less attachment (LF 16 kHz). Line traces represent mean ± s.d. for 9 wells per condition; bar graphs are at 48 hours (***, $p < 0.0001$, $n = 9$ wells). **d**, Co-culture sensitivity was characterized by mixing two breast cancer cell types of differing functional properties, MCF-7 and MDA-MB-231, plated at a total of 10,000 cells/well. Gradients correlating to plating ratios are observed for cell size (VF 16 kHz) and RMS (movement). Line traces represent mean ± s.d. for 12 wells per condition.

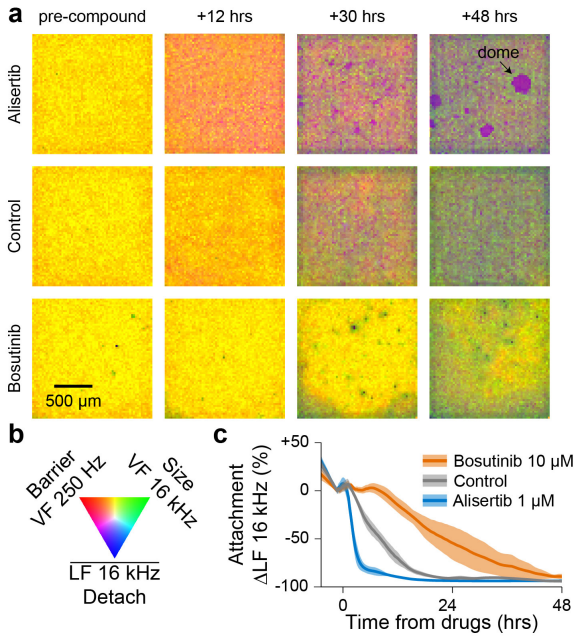

Fig. 4 | Water transport phenotype for ADPKD drug discovery applications. a-b, A set of 10 compounds were tested against the water transport phenotype exhibited in MDCK (canine kidney) cells; Supplementary Video 2 shows the full 96-well CMOS microplate video. Select time point electrochemical images for 1 of 3 replicates for Alisertib (1 µM) and Bosutinib (10 µM) are shown in (a) with a colormap in (b). Domes were only observed for tissues treated with Alisertib. **c**, Line traces show Alisertib accelerated and Bosutinib delayed the water transport detachment (LF 16 kHz) with respect to the control; mean ± s.d. for 3 wells per condition. The differential results match animal study results (Main text) for autosomal dominant polycystic kidney disease (ADPKD), suggesting the water transport phenotype could be predictive of ADPKD efficacy.

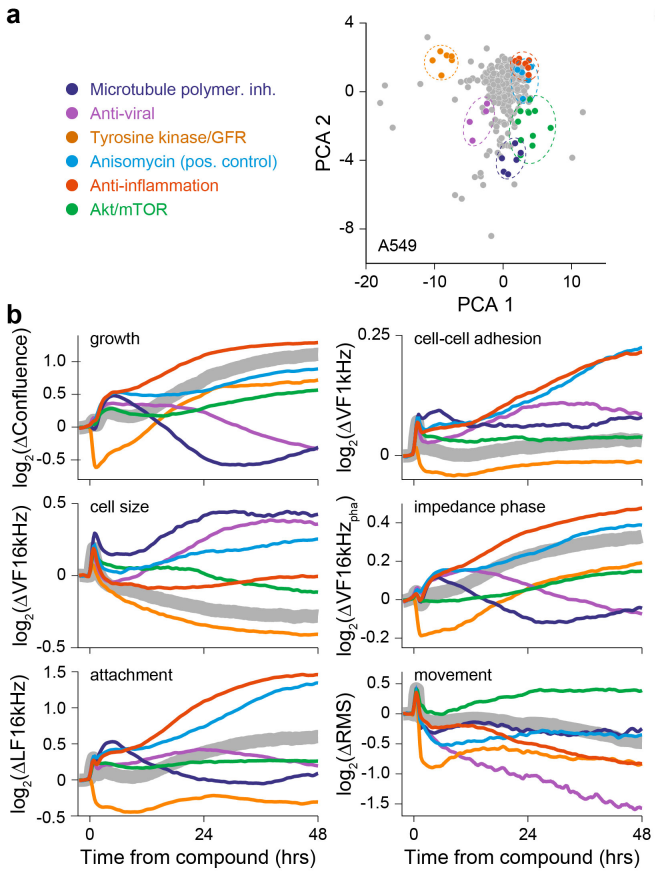

c

Cluster	Compound name	Target/pathway
Positive control	Anisomycin - plate 1	JNK activator/pos. control
	Anisomycin - plate 2	JNK activator/pos. control
	Anisomycin - plate 3	JNK activator/pos. control
	Anisomycin - plate 4	JNK activator/pos. control
	Anisomycin - plate 5	JNK activator/pos. control
Anti-inflammation	Drostanolone Propionate	Androgen Receptor
	Desoximetasone	Glucocorticoid Recep
	Tannic acid	CXCR
	Clofazimine	Phospholipase (e.g. PLA)
	Dexamethasone (DHAP)	Autophagy,IL Receptor
	Dexamethasone Acetate	Autophagy,IL Receptor
	Pinaverium bromide	Calcium Channel
Akt/mTOR	Lenvatinib (E7080)	Protein Tyrosine Kinase
	Bleomycin sulfate	DNA/RNA Synthesis
	Roxadustat (FG-4592)	HIF/Angiogenesis
	Ribociclib (LEE011)	CDK/Cell Cycle
	Rapamycin (Sirolimus)	PI3K/Akt/mTOR
	Zotarolimus(ABT-578)	PI3K/Akt/mTOR
	Ridaforolimus (Deforoli...	PI3K/Akt/mTOR
	Temsirolimus (CCI-779...	PI3K/Akt/mTOR
	Everolimus (RAD001)	PI3K/Akt/mTOR
	Fingolimod (FTY720) HCl	GPCR & G Protein
	Fingolimod	GPCR & G Protein
Microtubule polymer inh.	Picropodophyllin (PPP)	IGF-1R
	Flubendazole	Autophagy
	Vincristine sulfate	Autophagy, Microtubule Asc.
	Monomethyl auristatin E	Microtubule Associated
	Combretastatin A4	Microtubule Associated
	HMN-214	PLK
Anti-Viral	Triptolide (PG490)	NF-κB/ Anti-viral
	Halofuginone	DNA/RNA Synthesis/ Anti-viral
	Harringtonine	Cancer/ Anti-viral
	Homoharringtonine	STAT/ Anti-viral
Tyrosine kinase inhibitors/GFR	Nintedanib (BIBF 1120)	PDGFR, FGFR, VEGFR, FLT3, Src
	Nintedanib Ethanes...	PDGFR, FGFR, VEGFR, FLT3, Src
	Bosutinib (SKI-606)	BCR-Abl, Src, PDGFR, VEGFR
	Vandetanib (ZD6474)	VEGFR, EGFR, RET
	Gilteritinib (ASP2215)	FLT3,TAM Receptor
	GS-9876 (Ianraplenib)	Syk

Fig. 5 | Multiparametric impedance measurements reveal phenotypic landscape of FDA approved compound effects. a, A549 (lung/alveoli) cells were treated with a library of 341 FDA approved compounds at a concentration of 10 µM; Anisomycin (100 nM) was used as a positive control. A principal component analysis (PCA) was performed using the various field measurements (VF, LF at 1 kHz, 4 kHz, and 16 kHz) and calculations (confluency, RMS) across time points spanning from 0 – 48 hours post compound treatment (see Methods). The first two dimensions of PCA space are displayed with select clusters highlighted. **b**, Time traces for 48 hours post compound treatment for a subset of the used parameters in the PCA show unique signatures for each of the clusters. Gray lines represent the control (median) response, while the clusters are distinguished using the colors from (a). **c**, Compounds for each displayed cluster with a target and/or pathway identified curated from the compound supplier.

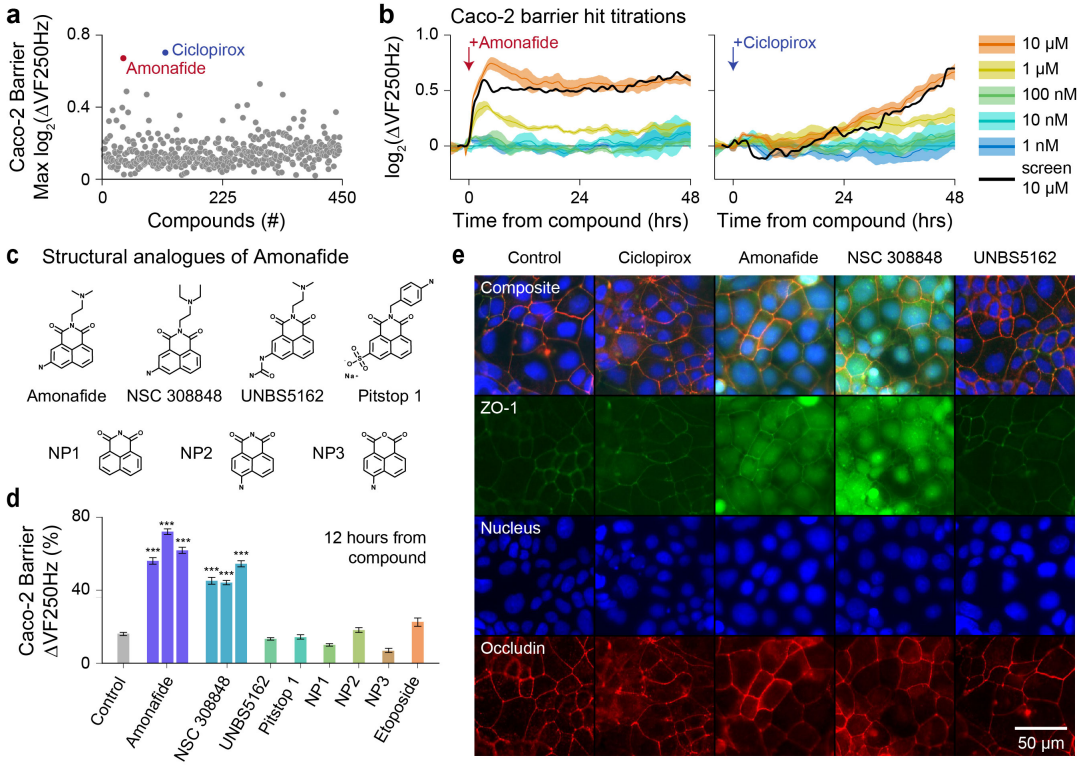

Fig. 6 | A FDA approved compound library screen reveals a new mechanism of action (MOA) for increasing barrier function using a Caco-2 gut model. a, A library of 341 FDA approved compounds were tested against the barrier function phenotype exhibited in Caco-2 (colon) cells; Supplementary Fig. 7 shows a principal component analysis of measured phenotypes. The max of the VF 250 Hz measurement from 0 – 48 hours post drug treatment was plotted to identify compounds which most increased the tissue barrier; screen performed at 10 μM. **b**, A dose response on Caco-2 tissues was performed for the highest observed increase in barrier, Amonafide and Ciclopirox. Concentrations were tested from 1 nM to 10 μM (traces are time normalized to control); the screen result is overlayed for comparison. The fast versus slow barrier increase for the two compounds suggests different mechanisms of action. Line traces represent mean ± s.d. for 3 wells per concentration. **c**, A Commercially available compounds with similar chemical structures to Amonafide. **d**, Multiple rounds of screenings show a rapid increase in barrier for

Amonafide and NSC 308848; all other compounds show no significant effect versus control. Bar graphs are at 12 hours (***, $p < 1e\text{-}5$, $n = 3$ wells). Etoposide represents a similar mechanism of action as Amonafide's specified Topoisomerase II inhibition but is not chemically similar. **e**, Immunofluorescence imaging was performed at 48 hours post compound treatment for Ciclopirox, Amonafide, and the most similar Amonafide derivatives, NSC 308848 and UNBS5162. Cells were stained for ZO-1 (green), a cell-cell adhesion and signaling protein, for DAPI/nucleus (blue), and Occludin (red), a cell-cell adhesion protein. Significant increases in ZO-1 in the membrane and nucleus are observed for both Amonafide and NSC 308848 (see Supplementary Fig. X for quantification). The localization of ZO-1 to the nucleus at 48 hours combined with the rapid increase in impedance barrier suggests an off-target MOA for Amonafide which directly tightens cell-cell junctions resulting in a ZO-1 signaling response.